

Environmental Breakdown of Topological Interface States in Armchair Graphene Nanoribbon Heterostructures: Is it true?

David M T Kuo

Department of Electrical Engineering and Department of Physics,
National Central University, Chungli, 32001 Taiwan

(Dated: January 27, 2026)

We investigate the environmental stability of topological interface states (IFs) in two sandwich nanostructures, BNNR/AGNRH/BNNR and BNNR/AGNRH/NBNR, where AGNRH denotes an armchair graphene nanoribbon heterostructure and BNNR (NBNR) represents a boron nitride nanoribbon. The former corresponds to a same-topology configuration, whereas the latter realizes a reverse-topology configuration. Using a bulk boundary perturbation approach, we show that in BNNR/AGNRH/BNNR the IFs are destroyed by chirality breaking induced by symmetric BN environments at both interfaces. In contrast, the IFs in the reverse-topology structure remain robust against lateral interface interactions from BN atoms. Transport calculations further demonstrate that the surviving IFs in BNNR/AGNRH/NBNR exhibit the characteristic behavior of topological double quantum dots, with an enhanced interdot hopping strength compared with vacuum boundary conditions. These results reveal that BN environments can either suppress or reinforce topological interface states, depending critically on the topology of the surrounding nanoribbons.

Introduction—Bottom-up synthesis techniques enable the fabrication of graphene nanoribbons (GNRs) with atomic precision [1–10]. Compared with zigzag GNRs (ZGNRs), armchair GNRs (AGNRs) exhibit tunable electronic phases [5], making them promising candidates for nanoelectronic applications [9]. More complex GNR architectures, including 9-7-9 and 7-9-7 armchair graphene nanoribbon heterostructures (AGNRHs) [10] and Janus GNR segments [11], have also been experimentally realized. Scanning tunneling microscopy measurements have confirmed the presence of topological states (TSs) in these systems, such as end states (ESs) and interface states (IFs) in 9-7-9 and 7-9-7 AGNRHs [10].

Although topological IFs in AGNRHs, such as 9-7-9 ribbons, have been extensively studied in idealized or substrate-agnostic models [10,12,13], the role of the environment particularly lateral embedding materials that break sublattice symmetry remains largely unexplored. In realistic device configurations, AGNRHs are inevitably coupled to surrounding materials, raising a critical question: are topological interface states robust against such environmental perturbations? Here, we theoretically investigate a 9-7-9 AGNRH laterally embedded in boron nitride nanoribbons (BNNRs), as illustrated in Fig. 1(a) and 1(b). Two distinct configurations are considered, in which the upper and lower BNNRs realize either the same-topology or reverse-topology scenario. Owing to the difficulty of employing density functional theory (DFT) to compute transmission coefficients in large 9-7-9-AGNRH/BNNR junctions [14–16], we adopt a tight-binding model combined with the Green function technique to evaluate quantum transport in AGNRHs embedded in BN environments [17,18].

Surprisingly, we find that BNNR/AGNRH/NBNR structures with reverse topology preserve the functionality of topological double quantum dots (TDQDs), in which a single energy level associated with each quantum dot remains well isolated from the bulk states.

Moreover, the electron hopping strength between the TDQDs is significantly enhanced compared with the vacuum boundary condition. This behavior is highly unusual when contrasted with conventional semiconductor double quantum dot (DQD) systems [19,20], whose operation is typically restricted to ultra-low temperatures due to the small energy separation between bound and continuum states. Nanoelectronic devices based on TDQDs therefore offer a promising route toward robust high-temperature quantum functionality.

Calculation Methodology—To investigate the transport properties of the BNNR/AGNRH/NBNR heterojunction connected to metallic electrodes, we employ a combination of a tight-binding model and the Green’s function technique [17]. The system Hamiltonian, illustrated in Fig. 1(b), is written as $H = H_0 + H_{GNR}$, where H_0 describes the electrodes and their coupling to the nanoribbon system, and H_{GNR} represents the BNNR/9-7-9-AGNRH/NBNR structure.

$$H_0 = \sum_k \epsilon_k a_k^\dagger a_k + \sum_k \epsilon_k b_k^\dagger b_k + \sum_\ell \sum_k V_{k,\ell,j}^L d_{\ell,j}^\dagger a_k + \sum_\ell \sum_k V_{k,\ell,j}^R d_{\ell,j}^\dagger b_k + h.c. \quad (1)$$

The first two terms describe free electrons in the left and right metallic electrodes. The operators a_k^\dagger (b_k^\dagger) create an electron with momentum k and energy ϵ_k in the left (right) electrode, respectively. The coupling amplitudes $V_{k,\ell,j=1}^L$ and $V_{k,\ell,j=M}^R$ describe tunneling between the left (right) electrode and its adjacent atom located in the ℓ -th row at the zigzag edge.

$$H_{GNR} = \sum_{\ell,j} E_{\ell,j} d_{\ell,j}^\dagger d_{\ell,j} - \sum_{\ell,j} \sum_{\ell',j'} t_{(\ell,j),(\ell',j')} d_{\ell,j}^\dagger d_{\ell',j'} + h.c. \quad (2)$$

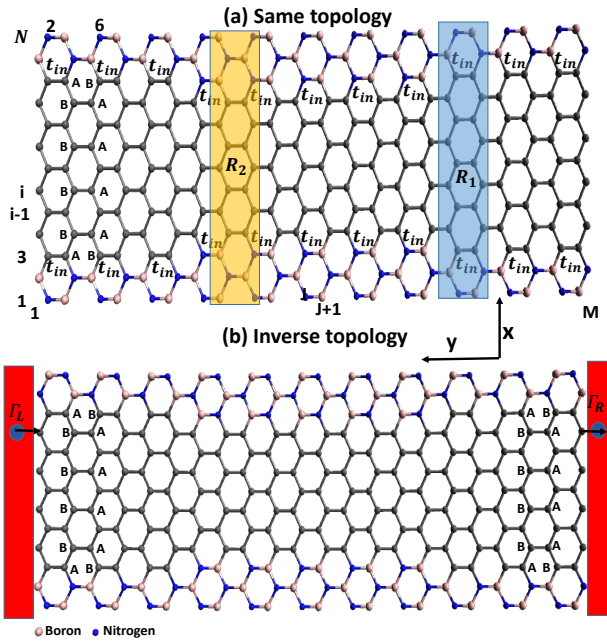


FIG. 1: Schematic illustration of an armchair graphene nanoribbon heterostructure (AGNRH) laterally embedded in a hexagonal boron nitride (BN) sheet, forming two distinct configurations: (a) a same-topology structure, 2-BNNR/9-7-9-AGNRH/2-BNNR, and (b) a reverse-topology structure, 2-BNNR/9-7-9-AGNRH/2-NBNR. White and blue sites denote boron and nitrogen atoms, respectively. R_1 and R_2 represent the unit cells (u.c.) of the 9-AGNR/2-BN and 7-AGNR/3-BN junctions, respectively. The tunable parameter t_{in} characterizes the interfacial coupling between the AGNRH and the BNNRs. The symbols Γ_L (Γ_R) represent the electron tunneling rates between the left (right) electrode and the leftmost (rightmost) atoms at the zigzag edges.

Here, $E_{\ell,j}$ denotes the on-site energy of the orbital at site (ℓ,j) , while $d_{\ell,j}^\dagger$ and $d_{\ell,j}$ are the electron creation and annihilation operators, respectively. The parameter $t_{(\ell,j),(\ell',j')}$ characterizes the hopping amplitude between sites (ℓ',j') and (ℓ,j) . For the BNNR/AGNRH/NBNR system, we assign on-site energies $E_B = \Delta_B$, $E_N = -\Delta_N$, and $E_C = 0$ for boron, nitrogen, and carbon atoms, respectively. Variations in hopping strengths between different atomic species are neglected, and the condition $E_B = -E_N = \Delta = 2.7$ eV is adopted for simplicity [21–24]. The nearest-neighbor hopping energy is set to $t_{(\ell,j),(\ell',j')} = t_{pp\pi} = 2.7$ eV.

To quantify interfacial interactions induced by the BN environment, we introduce an inter-nanoribbon hopping parameter t_{in} based on bulk boundary perturbation approach[12], as illustrated in Fig. 1(a). When $t_{in} = 0$, the BNNR/AGNRH/BNNR (or BNNR/AGNRH/NBNR) structure is decoupled into three isolated segments—the bottom BNNR, the central

9-7-9-AGNRH, and the top BNNR (or NBNR)—each subject to vacuum boundary conditions. Varying t_{in} effectively models different strengths of lateral interface interactions arising from surrounding two-dimensional insulating environments [25].

The bias-dependent transmission coefficient $T_{GNR}(\varepsilon)$ is calculated using $T_{GNR}(\varepsilon) = 4Tr[\Gamma_L(\varepsilon)G^r(\varepsilon)\Gamma_R(\varepsilon)G^a(\varepsilon)]$ [13], where $\Gamma_L(\varepsilon)$ and $\Gamma_R(\varepsilon)$ denote the tunneling rate (in energy units) at the left and right leads, respectively, and $G^r(\varepsilon)$ and $G^a(\varepsilon)$ are the retarded and advanced Green's functions of the GNRs, respectively. In terms of tight-binding orbitals, $\Gamma_\alpha(\varepsilon)$ and Green's functions are matrices. The expression for $\Gamma_{L(R)}(\varepsilon)$ is derived from the imaginary part of the self-energies, denoted as $\Sigma_{L(R)}^r(\varepsilon)$, and is given by $\Gamma_{L(R)}(\varepsilon) = -\text{Im}(\Sigma_{L(R)}^r(\varepsilon)) = \pi \sum_k |V_{k,\ell,j=1(M)}^{L(R)}|^2 \delta(\varepsilon - \epsilon_k)$. In the wide-band limit, $\Gamma_{L(R)}(\varepsilon)$ is replaced by an energy-independent constant matrix $\Gamma_{L(R)}$ [12].

Results and discussion—Interface-induced modifications of armchair AGNRs embedded in BN sheets have been experimentally observed and shown to alter the band gaps between conduction and valence subbands [26–29]. To elucidate how BN environments affect the topological IFs of 9-7-9-AGNRHs, we first examine the influence of BNNRs with different topologies on individual 7-AGNR and 9-AGNR with R_1 unit cells. Figures 2(a) and 2(b) show the calculated band structures of 4-BNNR/7-AGNR/4-BNNR and 4-BNNR/9-AGNR/4-BNNR, corresponding to same-topology configurations. The resulting band gaps are 1.22 eV and 1.19 eV, respectively, compared with 1.0 eV and 0.9 eV for isolated 7-AGNR and 9-AGNR under vacuum boundary conditions. These results indicate that BN embedding induces only weak perturbations to the bulk electronic structure when the surrounding BNNRs share the same topology[18,24].

In contrast, for inverse-topology configurations shown in Figs. 2(c) and 2(d), the band gaps of 4-BNNR/7-AGNR/4-NBNR and 4-BNNR/9-AGNR/4-NBNR are significantly reduced to 0.394 eV and 0.454 eV, respectively. This pronounced gap renormalization highlights the strong influence of BN environments when the bottom BNNR has opposite topology to the top NBNR. These tight-binding results are in good agreement with previous DFT calculations [18,24], and the small residual differences suggest that higher-order hopping processes play a negligible role in the low-energy conduction and valence subbands. We further find that varying the BNNR width ($n = 6, 8, 10, \dots$) does not qualitatively alter the band-edge dispersions, justifying the use of 4-BNNRs in the following analysis.

In realistic experiments, AGNR and AGNRH segments have finite lengths, typically below 20 nm[10]. We therefore examine the discrete energy spectra of finite 7-AGNR and 9-7-9 AGNRH segments embedded in BN environments with same and inverse topology, as shown in Fig. 3. Figures 3(a) and 3(b) display the energy lev-

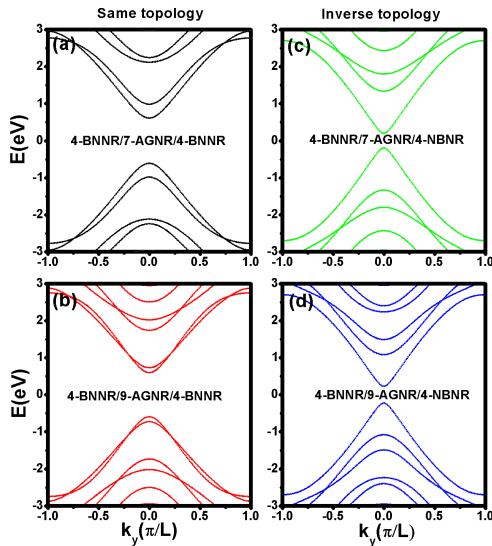


FIG. 2: Quasi-1D electronic band structures of AGNRs embedded in hexagonal BN sheets. Same-topology configurations: (a) 4-BNNR/7-AGNR/4-BNNR and (b) 4-BNNR/9-AGNR/4-BNNR. Inverse-topology configurations: (c) 4-BNNR/7-AGNR/4-NBNR and (d) 4-BNNR/9-AGNR/4-NBNR. We have adopted $t_{in} = 2.7$ eV and $\Delta = 2.7$ eV. L is the length of R_1 unit cell.

els of 4-BNNR/7-AGNR/4-BNNR and 4-BNNR/9-7-9-AGNRH/4-BNNR as functions of the interfacial hopping strength t_{in} for the same-topology case. Owing to the finite size of the 7-AGNR segment ($N = 15, M = 80$), two in-gap energy levels labeled $\Sigma_{ES,C}$ and $\Sigma_{ES,V}$ emerge from ESs, as shown in Fig. 3(a). In the absence of BN coupling ($t_{in} = 0$), these ESs form near-zero-energy modes. As t_{in} increases, $\Sigma_{ES,C}$ and $\Sigma_{ES,V}$ are strongly shifted away from zero energy, whereas the bulk states remain largely unaffected, consistent with the infinite-length results in Fig. 2.

Figure 3(b) reveals four in-gap energy levels originating from two ESs and two IFs in the 9-7-9 AGNRH segment. The IFs arise from the effective end states of the central 7-AGNR segment with R_2 unit cells, as discussed in our previous work[12]. Within the physically relevant range $0.8 t \leq t_{in} \leq t$, corresponding to realistic BN coupling strengths, the IF levels $\Sigma_{IF,C(V)}$ are no longer well isolated from the bulk states. This behavior contrasts sharply with the $t_{in} = 0$ limit and reflects the breakdown of topological protection due to chirality mixing induced by the symmetric BN environment.

The situation changes dramatically in the inverse-topology configuration shown in Figs. 3(c) and 3(d), where finite 7-AGNR and 9₆-7₈-9₆ AGNRH segments are embedded between a BNNR and an NBNR. Although the bulk band gap ($E_g = E_C - E_V$) is strongly reduced for $0.8 t \leq t_{in} \leq t$, the energy levels associated with ESs and

IFs in the 9-7-9 AGNRH remain nearly unchanged and well separated from the bulk continuum. This robustness is highly nontrivial, demonstrating that inverse topology effectively protects the IFs against strong environmental perturbations.

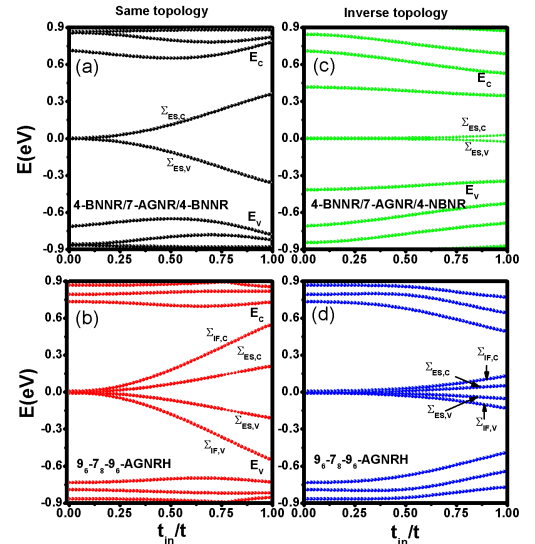


FIG. 3: Energy spectra of finite AGNR (AGNRH) segments as functions of interfacial hopping t_{in} at $\Delta = 2.7$ eV. Same-topology scenario: (a) 4-BNNR/7-AGNR/4-BNNR and (b) 4-BNNR/9-7-9-AGNRH/4-BNNR. Inverse-topology scenario: (c) 4-BNNR/7-AGNR/4-NBNR and (d) 4-BNNR/9-7-9-AGNRH/4-NBNR.

To clarify the contrasting behaviors observed in Figs. 3(b) and 3(d), we plot the charge densities of $\Sigma_{IF,C}$ for different t_{in} values in Fig. 4. For $t_{in} = 0$, shown in Fig. 4(a), the AGNRH is completely decoupled from the BN environment, corresponding to vacuum boundary conditions. The state $\Sigma_{IF,C}$ arises from the coupling between a left IF with A-sublattice chirality ($\Psi_{IF,A}$) and a right IF with B-sublattice chirality ($\Psi_{IF,B}$), resulting in spatially separated charge densities and long-range hopping characteristic of topological states. When a small coupling $t_{in} = 0.2 t$ is introduced, the IF wave functions partially penetrate into the BN regions [Fig. 4(b)], leading to weak chirality perturbations. Even for strong coupling $t_{in} = 0.8 t$, shown in Fig. 4(c), the IF wave functions remain predominantly sublattice polarized, with only minor overlap between A and B sublattices.

In stark contrast, Figs. 4(d)-4(f) show that for same-topology configurations the IF charge densities become strongly polarized and localized at a single interface, accompanied by substantial overlap between opposite chiralities. This behavior indicates that the symmetric BN environment induces an effective lateral field along the armchair direction, breaking chirality and destroying the topological nature of the IFs.

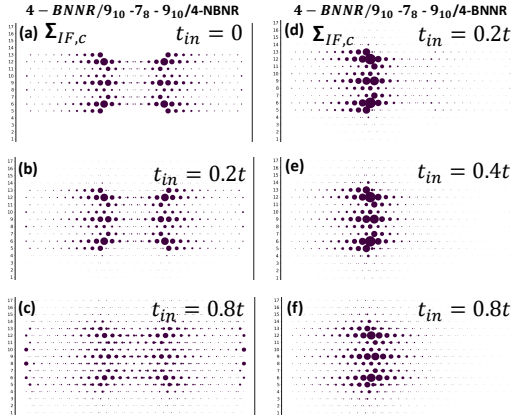


FIG. 4: Charge densities of the interface state $\Sigma_{IF,C}$ in $9_{10} - 7_8 - 9_{10}$ -AGNRH embedded in BN at $\Delta = 2.7$ eV. (a)-(c) Inverse-topology: $t_{in} = 0$ ($\Sigma_{IF,C} = 7.53$ meV), $t_{in} = 0.2t$ ($\Sigma_{IF,C} = 8.81$ meV), $t_{in} = 0.8t$ ($\Sigma_{IF,C} = 50.96$ meV). (d)-(f) Same-topology: $t_{in} = 0.2t$ ($\Sigma_{IF,C} = 31.35$ meV), $t_{in} = 0.4t$ ($\Sigma_{IF,C} = 117.57$ meV), $t_{in} = 0.8t$ ($\Sigma_{IF,C} = 0.402$ eV).

Finally, we examine the transport consequences of the robust IFs in inverse-topology structures. Figure 5 shows the calculated transmission coefficient $\mathcal{T}_{GNR}(\varepsilon)$ for 4-BNNR/96-78-96-AGNRH/4-NBNR at various t_{in} . Pronounced transmission peaks at $\Sigma_{IF,C}$ and $\Sigma_{IF,V}$ confirm that the system functions as a topological double quantum dot (TDQD). In contrast, no transport signatures are observed for ES-related energy levels, consistent with their short decay lengths compared with the channel length ($M = 80$). The transmission spectra near the IF resonances are well described by $\mathcal{T}_{TDQD}(\varepsilon) = \frac{4\Gamma_{e,L}t_x^2\Gamma_{e,R}}{|(\varepsilon-E_L+i\Gamma_{e,L})(\varepsilon-E_R+i\Gamma_{e,R})-t_x^2|^2}$ in the absence of inter-dot and intra-dot Coulomb interactions[30], where $\Gamma_{e,L(R)}$ denotes the effective tunneling rate between the electrodes and the left (right) TQD, $E_{L(R)} = 0$, and t_x is the interdot hopping strength. The zero-temperature electrical conductance $G_e(\mu) = (2e^2/h)\mathcal{T}_{GNR}(\varepsilon = \mu)$ reaches the conductance quantum $G_0 = 2e^2/h$ at the energy levels of $\Sigma_{IF,C}$ and $\Sigma_{IF,V}$. Notation μ is Fermi energy of the electrodes. Notably, the spectra of $G_e(\mu)$ indicate that the effective hopping t_x between IFs in inverse-topology BN environments is enhanced relative to the vacuum boundary condition, underscoring the constructive role of topology-engineered environments in stabilizing and strengthening topological transport.

Conclusion—In this work, we theoretically investigated the transport properties of 9-7-9 AGNRH laterally embedded in boron nitride (BN) sheets. Two sandwich configurations were considered, n -BNNR/AGNRH/ n -BNNR and n -BNNR/AGNRH/ n -NBNR, corresponding to same-topology and reverse-topology environments, respectively. These distinct topological scenarios lead to fundamentally different behaviors of the end states (ESs) and interface states (IFs) in the AGNRH.

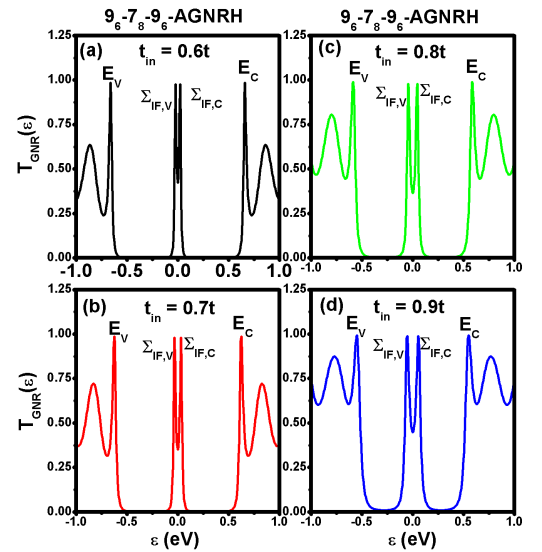


FIG. 5: Transmission coefficients $\mathcal{T}_{GNR}(\varepsilon)$ of the 4-BNNR/96-78-96-AGNRH/4-NBNR structure for various t_{in} at $\Gamma_t = 2.7$ eV. (a) $t_{in} = 0.6t$, (b) $t_{in} = 0.7t$, (c) $t_{in} = 0.8t$, and (d) $t_{in} = 0.9t$.

For same-topology BN environments, interfacial interactions between BN and C atoms strongly break the chirality of the IFs, resulting in the destruction of their topological character. In contrast, when the surrounding BN nanoribbons realize a reverse-topology configuration, the IF chirality is only weakly perturbed, allowing the IFs in n -BNNR/9-7-9-AGNRH/ n -NBNR to retain the functionality of TDQDs, with energy levels that remain well isolated from the bulk states. Within a bulk boundary perturbation framework, we further demonstrate that these IFs are robust not only under vacuum boundary conditions but also against strong lateral interface interactions.

Our results establish topology-engineered BN environments as an effective route to stabilizing and even enhancing topological interface states in AGNRHs. Such symmetry-protected IFs provide a promising platform for realizing robust quantum functionalities, including high-temperature quantum-dot and qubit-like applications, in graphene-based nanoelectronic devices.

Acknowledgments

This work was supported by the National Science and Technology Council, Taiwan under Contract No. MOST 107-2112-M-008-023MY2.

E-mail address: mtkuo@ee.ncu.edu.tw

¹ J. Cai, P. Ruffieux, R. Jaafar, M. Bieri, T. Braun, S. Blankenburg, M. Muoth, A. P. Seitsonen, M. Saleh, X. Feng, K. Mullen and R. Fasel, Atomically precise bottom-up fabrication of graphene nanoribbons, *Nature*, **466**, 470 (2010).

² J. Z. Liu, B. W. Li, Y. Z. Tan, A. Giannopoulos, C. Sanchez-Sanchez, D. Beljonne, P. Ruffieux, R. Fasel, X. L. Feng and K. Mullen, Toward Cove-Edged Low Band Gap Graphene Nanoribbons, *J. Am. Chem. Soc.*, **137**, 6097 (2015).

³ Y. C. Chen, T. Cao, C. Chen, Z. Pedramraz, D. Haberer, D. G. de Oteyza, R. Fischer, S. G. Louie and M. F. Crommie, Molecular bandgap engineering of bottom-up synthesized graphene nanoribbon heterojunctions, *Nat. Nanotechnol.*, **10**, 156 (2015).

⁴ P. Ruffieux, S. Y. Wang, B. Yang, A. Sanchez, J. Liu, T. Dienel, L. Talirz, P. Shinde, C. Pignedoli, D. Passerone, T. Dumslaff, X. L. Feng, K. Mullen and R. Fasel, On-surface synthesis of graphene nanoribbons with zigzag edge topology, *Nature*, **531**, 489 (2016).

⁵ J. P. Llinas, A. Fairbrother, G. Borin Barin, W. Shi, K. Lee, S. Wu, B. Y. Choi, R. Braganza, J. Lear, N. Kau et al. Short-channel field-effect transistors with 9-atom and 13-atom wide graphene nanoribbons. *Nat. Commun.*, **8**, 633 (2017).

⁶ P. H. Jacobse, A. Kimouche, T. Gebraad, M. M. Ervasti, J. M. Thijssen, P. Liljeroth, and I. Swart, Electronic components embedded in a single graphene nanoribbon. *Nat. Commun.*, **8**, 119 (2017).

⁷ L. Y. Lee, F. Z. Zhao, T. Cao, I. Jisoon and S. G. Louie, Topological Phases in Cove-Edged and Chevron Graphene Nanoribbons: Geometric Structures, Z(2) Invariants, and Junction States, *Nano Lett.* **18**, 7274 (2018).

⁸ D. J. Rizzo, G. Veber, J. W. Jiang, R. McCurdy, T. Bronner, T. Cao, T. Chen, S. G. Louie, F. R. Fischer and M. F. Crommie, Inducing metallicity in graphene nanoribbons via zero-mode superlattices, *Science*, **369**, 1597 (2020).

⁹ H. M. Wang, H. S. Wang, C. X. Ma, L. X. Chen, C. X. Jiang, C. Chen, X. M. Xie, A. P. Li and X. R. Wang, Graphene nanoribbons for quantum electronics, *Nat. Rev. Phys.* **3**, 791 (2021).

¹⁰ D. J. Rizzo, J. W. Jiang, D. Joshi, G. Veber, C. Bronner, R. A. Durr, P. H. Jacobse, T. Cao, A. Kalayjian, H. Rodriguez, P. Butler, T. Chen, S. G. Louie, F. R. Fischer and M. F. Crommie, Rationally Designed Topological Quantum Dots in Bottom-Up Graphene Nanoribbons, *ACS Nano*, **15**, 20633 (2021).

¹¹ S. T Song, Y. Teng, W. C. Tang, Z. Xu, Y. Y. He; J. W. Ruan, T. Kojima, W. P. Hu, F. J. Giessibl, H. Sakaguchi, S. G. Louie, and J. Lu, Janus graphene nanoribbons with localized states on a single zigzag edge, *Nature*, **637**, 580 (2025).

¹² David M. T. Kuo, Topological Interface States and Non-linear Thermoelectric Performance in Armchair Graphene Nanoribbon Heterostructures, *RSC Adv.*, **16**, 4680 (2026).

¹³ David M. T. Kuo, Room-Temperature Pauli Spin Blockade and Current Rectification in 15-13-15 Armchair Graphene Nanoribbon Heterostructures, *Nanoscale* **17**, 18920 (2025).

¹⁴ Y. W. Son, M. L. Cohen, and S. G. Louie, Energy Gaps in Graphene Nanoribbons, *Phys. Rev. Lett.*, **97**, 216803 (2006).

¹⁵ Y. Matsuda, W. Q. Deng and III W A Goddard, Contact Resistance for "End-Contacted" Metal-Graphene and Metal-Nanotube Interfaces from Quantum Mechanics, *J. Phys. Chem. C*, **114**, 17845 (2010).

¹⁶ V. T. Nikita, M. Ruize, L. Johannes, K. Efthimios, A. M. Arash, and P. Michele, Dirac Half-Semimetallicity and Antiferromagnetism in Graphene Nanoribbon/Hexagonal Boron Nitride Heterojunctions, *Nano Lett.*, **23**, 6698 (2023).

¹⁷ Z. H. Qiao, J. Jung and A. H. MacDonald, Electronic Highways in Bilayer Graphene, *Nano Lett.*, **11**, 3453 (2011).

¹⁸ J. Jung, Z. H. Qiao, Q. Niu, and A. H. MacDonald, Transport Properties of Graphene Nanoroads in Boron Nitride Sheets, *Nano Lett.*, **12**, 2936 (2012).

¹⁹ K. Ono, D. G. Austing, Y. Tokura and S. Tarucha, Current Rectification by Pauli Exclusion in a Weakly Coupled Double Quantum Dot System, *Science*, **297**, 1313 (2002).

²⁰ W. G. van der Wiel, S. De Franceschi, J. M. Elzerman, T. Fujisawa, S. Tarucha, and L. P. Kouwenhoven, Electron transport through double quantum dots, *Rev. Mod. Phys.*, **75**, 1 (2003).

²¹ Y. Ding, Y. Wang and J. Ni, Electronic properties of graphene nanoribbons embedded in boron nitride sheets, *Appl. Phys. Lett.*, **95**, 123105 (2009).

²² J. M. Pruneda, Origin of half-semimetallicity induced at interfaces of C-BN heterostructures, *Phys. Rev. B*, **81**, 161409(R) (2010).

²³ G. S. Seal and J. Guo, Bandgap opening in boron nitride confined armchair graphene nanoribbon, *Appl. Phys. Lett.*, **98**, 143107 (2011).

²⁴ S. Junghawan, S. Limpijumnong and J. L. Kuo, Electronic structures of graphene/boron nitride sheet superlattices, *Phys. Rev. B* **84**, 235424 (2011).

²⁵ D. P. Gorony, M. Ebrahimi, F. Rosi, Arramel, Y. Fang, S. De Feyter, C. Wang, P. H. Beton, A. T. S. Wee, P. S. Weiss and D. F. Perepichka, Supramolecular Assemblies on Surfaces: Nanopatterning, Functionality and Reactivity, *ACS Nano*, **12**, 7445 (2018).

²⁶ M. P. Levendorf, C. J. Kim, L. Brown, P. Y. Huang, R. W. Havener, D. A. Muller and J. Park, Graphene and boron nitride lateral heterostructures for atomically thin circuitry, *Nature*, **488**, 627 (2012).

²⁷ L. X. Chen, L. He, H. S. Wang, H. M. Wang, S. J. Tang, C. X. Cong, H. Xie, L. Li, H. Xia, and T. X. Li, Oriented graphene nanoribbons embedded in hexagonal boron nitride trenches, *Nat. Commun.*, **8**, 14703 (2017).

²⁸ H. S. Wang; L. X. Chen, K. Elibol, L. He, H. M. Wang, C. Chen, C. X. Jiang, C. Li, T. R. Wu, and C. X. Cong, Towards chirality control of graphene nanoribbons embedded in hexagonal boron nitride, *Nat. Mater.*, **20**, 202 (2021).

²⁹ D. C. Geng, I. Abdelwahab, X. F. Xiao, A. Cernescu, W. Fu, V. Giannini, S. A. Maier, L. Li, W. P. Hu, and K. P. Loh, One-Pot Confined Epitaxial Growth of 2D Heterostructure Arrays, *ACS. Materials Lett.*, **3**, 217 (2021).

³⁰ David M. T. Kuo, Temperature-stable tunneling current in serial double quantum dots: insights from nonequilibrium green functions and Pauli spin blockade, *Phys. Chem. Chem. Phys.*, **27**, 5238 (2025).